Coupling Light with Matter for Identifying Dominant Subnetworks

Airat Kamaletdinov and Natalia G. Berloff*

Department of Applied Mathematics and Theoretical Physics,
University of Cambridge, Cambridge CB3 0WA, United Kingdom
(Dated: May 28, 2024)

We present a novel light-matter platform that uses complex-valued oscillator networks, a form of physical neural networks, to identify dominant subnetworks and uncover indirect correlations within larger networks. This approach offers significant advantages, including low energy consumption, high processing speed, and the immediate identification of co- and counter-regulated nodes without post-processing. The effectiveness of this approach is demonstrated through its application to biological networks, and we also propose its applicability to a wide range of other network types.

Recent advancements have led to developing specialized computing architectures designed to tackle optimization challenges and enhance machine learning processes. These architectures acting as physical neural networks (PNNs) exploit various physical principles to efficiently guide systems toward equilibrium states. Fundamental principles include thermal annealing and its derivatives, quantum annealing, Hopf bifurcation at the condensation threshold, minimum power dissipation, the principle of least action, and minimum entropy generation [1]. These principles form the foundation of efficient physics-inspired computing heuristics, known as π-computing. These heuristics are then translated into conventional computational algorithms, enabling more effective and efficient problem-solving capabilities.

Coupled light-matter complex-valued neural networks, a type of PNNs, present an innovative approach to computing, distinct from traditional gate-based methods and annealing techniques, both quantum and classical. Among these, exciton-polariton condensates are particularly noteworthy as they epitomize the coupling of light and matter. They give rise to Gain-Based Computing (GBC), which relies on the interplay of light and matter, employing advanced laser technologies and spatial light modulators (SLMs) to facilitate parallel processing across numerous channels, assisted by the nonlinearities intrinsic to the matter component, and achieving exceptional energy efficiency.

At the heart of GBC is a unique operational sequence where an increase in gain power is coupled with symmetry breaking and gradient descent mechanisms. This process involves waves' inherent coherence and synchronization, naturally guiding the system towards a state of minimized losses. In this context, fully exploiting light's degrees of freedom — amplitudes and phases — potentially should enable richer computational capabilities in photonic or polaritonic complex-valued neural networks, enhancing their ability to process and interpret complex data patterns efficiently.

Recent advancements in GBC-inspired hardware have introduced a variety of technologies. These include coherent Ising machines (CIMs) based on optical parametric oscillators (OPOs) [2–5], advanced laser systems [6–8], photonic simulators [9, 10], polariton [11, 12] and photon condensates [13]. The primary focus of these approaches is to solve optimisation problems on a set of either discrete or continuous variables that can be mapped onto the phases of generally complex signal amplitudes so that the goal is limited to finding the ground state of various classical spin Hamiltonians such as Ising, XY, Clock, k-local, etc. [14]. However, supporting only the problems that can be mapped into a standard spin Hamiltonian restricts the scope of applications that can be efficiently embedded in the physical hardware or algorithms. Notably, there have been several proposals to extend the class of Ising Hamiltonians to mixed-integer or box-constrained quadratic optimisation problems [15–17].

In our Letter, we show that the amplitudes and phases of complex-valued oscillators can be exploited to solve the problem of identifying a dominant subnetwork—a problem central to network analysis. By engaging all degrees of freedom, our method enables a more direct representation and processing of data.

Identifying subnetworks of closely interacting nodes can provide valuable insight into the structure and function of complex systems. For example, in social networks, identifying sub-communities can help understand how information spreads within the network and how different groups interact. In financial networks, identifying clusters of companies or markets can help understand how different sectors of the economy are interconnected and how they influence each other. In transportation networks, identifying clusters of locations can help optimise transportation routes and improve efficiency. Identifying groups of devices or users in communication networks can help improve network performance and reliability. The analysis of subnetworks within complex bio-molecular networks offers valuable insights into the intricate patterns of cellular interactions, particularly in the context of temporal and condition-specific conditions. Extracting condition-specific subnetworks is crucial in understanding cellular adaptations to environmental changes and gene expression alterations associated with diseases and ageing. Bio-molecular networks were constructed by integrating multiple microarray data sets, considering the

* correspondence address: N.G.Berloff@damtp.cam.ac.uk

interplay between genes and their expressions and combining these with other data sets such as protein-protein or protein-DNA interaction into a single coupling matrix $\mathbf{J}$, with components J_{ij} that characterize the strength and kind (positive or negative) of the correlations between i–th and j–th genes.

There are different ways to define the dominant subnetwork given the coupling matrix $\mathbf{J}$. One common approach is to find the principle eigenvector of $\mathbf{J}$ that gives the steady-state distribution of a Markov chain in a random walk model where transition probabilities are proportional to the weights of the edges. Hence, nodes with high values in the dominant eigenvector are those with strong connections to other influential nodes. However, this does not lead to the true dominant subnetwork that is usually defined as a clique (a portion of the graph where every node is connected to every other node within that same subset, forming a complete subgraph) with the highest total edge weight among all cliques in the graph [18]. Such a problem is known as a Maximum Weighted Clique Problem (MWCP) and is nondeterministic polynomial (NP)-hard. There are no efficient algorithms for solving MWCP on large-scale networks, so traditional algorithms must be revised due to their substantial space and time complexity [19]. For instance, conventional approaches frequently rely on an adjacency matrix to expedite operations like verifying adjacency between two vertices untenable for large-scale graphs. Similarly, the prevailing algorithms typically do not exhibit the low time complexity necessary for efficiently processing large-scale graphs. This deficiency hampers their applicability in scenarios where rapid analysis of large graphs is crucial. In this light, it is essential to allow physical systems to navigate the complexities of massive graphs with enhanced efficiency and lower computational demands.

MWCP can be formulated as a continuous optimization problem [18] using the exact Motzkin-Straus mapping between maximum clique optimizations problem and continuous quadratic optimisation [20]. The formulation of this problem can be stated as follows:

$$\max_{x_i \geq 0} \sum_i \sum_{j<i} |J_{ij}| x_i x_j, \quad \text{subject to} \quad \sum_i x_i = 1, \quad (1)$$

where $i = 1, ..., N$, N is the network size, $x_i \in \mathbb{R}$ is the node's importance in the network, and the condition $\sum_i x_i = 1$ maximises the interconnectivity of subnetwork. Note that if the graph is unweighted ($|J_{ij}| = 1$), the optimizers become $x_i = 1/\eta$ if the i–th node belongs to MWC of size η and $x_i = 0$ otherwise [20].

Now, we formulate the "Optical DOMInant subNetwork detection" platform "DOMINO" and demonstrate its application to real biological gene-gene coexpression networks. In Eq. (1), we take the modulus of the coupling strengths J_{ij} as it corresponds to the strength of the interactions (positive or negative). After identifying the dominant subnetwork, we show that the same optical platform can detect indirect correlations in networks and quantify the strength and direction of these correlations between nodes.

Optical DOMInant subNetwork detection - DOMINO. To construct the optical GBC platform that solves MWCP of Eq. (1), we consider the network of coupled condensates or lasers, a practical realization of PNNs, with the state of the i–th condensate described by the wavefunction $\psi_i(t) = |\psi_i| \exp[i\theta_i]$ with phase θ_i relative to a reference condensate in a fast reservoir regime as

$$\frac{d\psi_i}{dt} = \gamma_i(t, |\psi_i|^2)\psi_i + \sum_{j=1}^{N} J_{ij}\psi_j. \quad (2)$$

This equation can be obtained as a tight binding approximation of the Ginzburg-Landau model [21] with the effective gain (injection minus linear and nonlinear losses) given by $\gamma_i(t, |\psi_i|^2)$ and the interactions between condensates by $\mathbf{J}$. The effective gain typically involves some form of a saturable nonlinearity, the simplest of which is $\gamma_i = \gamma_{\text{inj}}^{(i)} - \gamma_{\text{loss}} - |\psi_i|^2$, with $\gamma_{\text{inj}}^{(i)} > 0$ and $\gamma_{\text{loss}} > 0$ being the injection rate and linear losses, respectively. Various types of feedback can be envisioned, in particular, the injection rate that itself depends on the condensate density

$$\frac{d\gamma_{\text{inj}}^{(i)}}{dt} = \epsilon(1 - |\psi_i|^2), \quad (3)$$

which for some positive parameter ϵ brings all condensate densities to the same value ($|\psi_i|^2 = 1$). With such feedback, the steady-state of Eq. (2) was shown to minimize the loss function $F_0 = \frac{1}{2}\sum_{i=1}^{N}(\gamma_{\text{inj}}^{(i)} - \gamma_{\text{loss}} - |\psi_i|^2)^2 - \frac{1}{2}\sum_{i,j} J_{ij}(\psi_i\psi_j^* + c.c.)$ and, therefore, the XY Hamiltonian $H_{XY} = -\frac{1}{2}\sum_{i,j} J_{ij}\cos(\theta_i - \theta_j)$ [22].

To solve MWCP Eq. (1) we propose to associate x_i with the amplitudes of ψ_i, assume that all condensates are phase-locked to the phase Φ of the reference condensate (so $\theta_i \to \theta_i - \Phi$) and consider the optical loss function

$$F_{\text{loss}} = \frac{1}{2}\sum_i \left(\xi - |\sum_j \psi_j|^2\right)^2 - \frac{1}{2}\sum_{i,j} |J_{ij}|(\psi_i\psi_j^* + c.c.), \quad (4)$$

where we modified F_0 by replacing the local $|\psi_i|^2$ term in the effective gain with the total light intensity $S = |\sum_j \psi_j|^2$. The first term in Eq. (4) becomes a penalty to violate the constraint $\sum_i x_i = 1$, dictated by Eq. (1).

Applying the Madelung transformation $\psi_i = \sqrt{\rho_i}\exp(i\theta_i)$ in Eq. (4) and letting $\theta_i \equiv \Phi$ for all i gives $F_{\text{loss}} = -\sum_{i<j} |J_{ij}|\sqrt{\rho_i\rho_j} + \frac{1}{2}\left(\xi - |\sum_j \sqrt{\rho_j}|^2\right)^2$. The global minimum of this loss function leads to the solution of Eq. (1) with amplitudes x_i mapped onto $\sqrt{\rho_i}$. Therefore, this functional can effectively encode MWCP. The system evolution to the minimum of F_{loss} follows $\dot{\psi}_i = -\partial F_{\text{loss}}/\partial\psi_i^*$, so that

$$\dot{\psi}_i = (\xi - |\sum_j \psi_j|^2)\psi_i + \sum_{i\neq j} Q_{ij}\psi_j. \quad (5)$$

This equation describes the dynamics of the optical system of the network of coupled condensates with coupling strengths $Q_{ij} = |J_{ij}| - |\sum_k \psi_k|^2 + \xi$.

In experiments, the losses proportional to the total light intensity $S = |\sum_j \psi_j|^2$ can be achieved either through the absorption of the excited states of the condensates by the intracavity layer, resulting in correct energy blueshift [23] or by measuring S and adjusting the laser intensity using a feedback scheme on the effective gain $\gamma_i(t)$. Experimentally, the injected light must stay coherent with the reference condensate to satisfy the condition $\sum_i \psi_i = e^{i\Phi} \sum_i \sqrt{\rho_i}$. This can be achieved by applying an external coherent optical field [24] or implementing a feedback control system that monitors the phase of each condensate [25]. Mathematically, we represent such coherence by adjusting the phases of $\psi_i(t)$ in Eq. (5) at each evolution step by the following feedback scheme (DOMINO)

$$\psi_i^{\text{new}} = \left| \psi_i^{\text{old}} + \Delta t \left((\xi - |\sum_j \psi_j^{\text{old}}|^2)\psi_i^{\text{old}} + \sum_{i<j} Q_{ij}\psi_j^{\text{old}} \right) \right|, \quad (6)$$

where ψ_j^{old} and ψ_j^{new} are separated by feedback time Δt. The gain-based schedule arising in Eq. (6) modifies the basins of attraction and allows the trajectories to depart from the direction of the primary eigenvector and directs the trajectory to the true global minimum as illustrated in Fig. 1. Fig. 1(a) shows the time evolution of amplitudes $|\psi_i|$ governed by Eq. (6). The insets in Fig. 1 demonstrate snapshots of the coupled condensate system at various times. Figure 1(b) shows histograms of solutions found by computer simulations of DOMINO (Eq. (6)) and its comparison with the 'BFGS' algorithm implemented via built-in 'scipy. optimise' library, as well as with solutions provided by the leading eigenvectors of the weights matrix $|J_{ij}|$ specified in Supp. Mat. A. One of the most critical advantages of DOMINO is the efficiency in navigating the basins of attraction towards the global minimum. This can be illustrated by comparing the number of different random initial conditions required to find the optimal solution using DOMINO and 'BFGS' method with the objective function $\min_{x_i} [-\sum_{ij} |J_{ij}|x_i x_j + 10(1 - \sum_i |x_i|)^2]$. DOMINO significantly exceeds the success probability of the 'BFGS' method, as shown in Fig. 1(c). Figure 2 shows the accumulated probability of success depending on the execution time for DOMINO and a state-of-the-art quadratic programming solver Gurobi [26] applied to the original formulation of Eq. (1). It can be seen that DOMINO finds a solution with better confidence faster than Gurobi for structured complex networks with a density $p > 0.05$. Supp. Mat. B illustrates the same behavior for randomly structured networks.

Any actual experimental realization of the physical solver will unavoidably operate with noisy data, primarily affecting coupling strengths J_{ij}. The ability to be robust to imperfections and the understanding of what level of errors leaves the solution stable plays an essential role in developing components of the actual physical
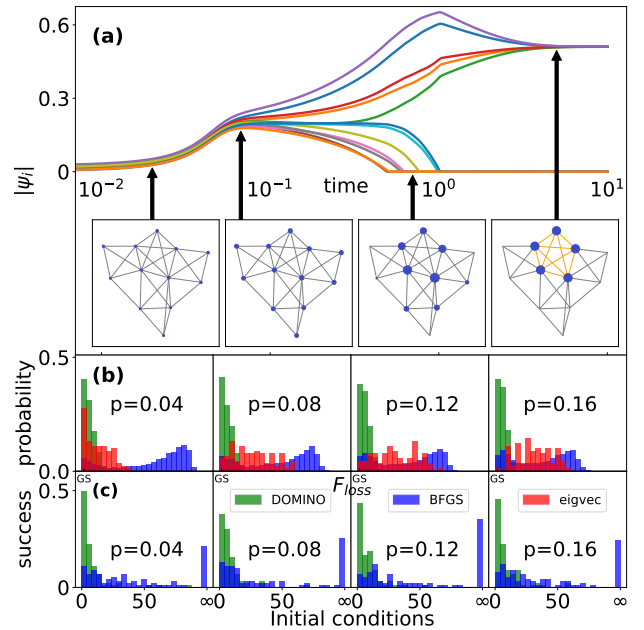

Figure 1. (a) Time evolution of amplitudes governed by Eq. (6) (with parameters $\xi = 5$ and $dt = 0.0005$) for the network shown in the most left inset with $|J_{ij}| = 1$ if there is an edge connecting i–th and j–th nodes and zero otherwise. The insets show snapshots of the system of coupled condensates at various moments in time. Only the nodes in the maximum clique have nonzero amplitudes at the end of the simulation, as shown in the most right inset. (b): histograms of the solutions found by the trajectories of DOMINO Eq. (6) (green) with parameters $\xi = 5, dt = 2 \cdot 10^{-4}$ and using 'BFGS' algorithm (blue). The red bars correspond to the solutions distribution provided by the leading eigenvectors of matrix $\mathbf{J}$. The histograms were calculated based on 100 connected random graphs of size $N = 100$ with different weights matrices J_{ij} generated for each of 100 different initial conditions for each graph. The leftmost bars correspond to the global minima, verified for each graph using the Gurobi solver. A detailed description of $\mathbf{J}$'s structure for each graph of density p is given in Supp. Mat A. (c): Number of different random initial conditions required to find the optimal solution using numerical integration of Eq. (6) calculated for 100 different connected random networks of size $N = 100$ with varying network densities p. Green bars correspond to solutions found by the DOMINO, and blue bars demonstrate convergence rates of the 'BFSG' algorithm. The values marked by ∞ show the fraction of networks G for which the ground state was not found for any of the 100 different initial conditions used.

solver. In Supp. Mat. C we show how the DOMINO solver resists noise and inaccuracies in natural physical systems. Simulations have demonstrated that even in conditions of noise reaching 5%, the errors remain within 3%. In Supp. Mat. D we estimate the energy and time efficiency of the DOMINO solver when implemented in optical hardware.

Gene-gene coexpression network. We applied our method to real-life biological data, specifically a gene-gene coexpression network [27]. This coexpression net-
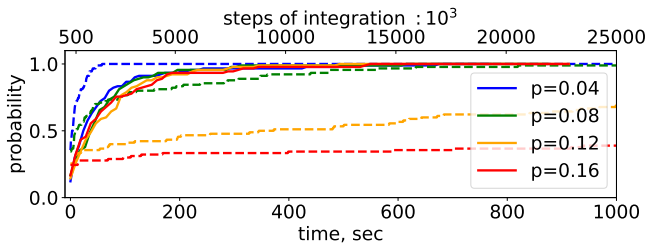
Figure 2. Comparison of the accumulated probability of success as a function of TTS for Gurobi (dashed lines) and DOMINO solver (Eq. (6) with $\xi = 5$ and $dt = 2 \cdot 10^{-4}$) (solid lines) for the networks of size $N = 100$. Both solvers are executed on the same single CPU core. DOMINO computation time was estimated as the time required to sequentially execute solver 100 times starting with different initial conditions. The upper axis shows the corresponding total number of steps of numerical integration of Eq. (6). The probability of success at each time step for both solvers was estimated as the fraction of 90 different matrices $\mathbf{J}$ for which a global minimum was found. A detailed description of $\mathbf{J}$'s structure for each graph of density p is given in Supp. Mat A.

work was established using the 3DCoop pipeline, which analyzed the occupancy profiles of 386 Transcription Regulators (TRs) in the K562 human myelogenous leukaemia cell line [28]. The 3DCoop pipeline leveraged peak information obtained from ChIP-seq experiments, indicating the precise locations where the protein of interest binds to the DNA within the cell. Utilising the information about how frequently these TRs bind to specific DNA locations within the cell as well as the spatial interactions between different genomic regions from Hi-C data, 3DCoop constructs TR-specific contact maps based on which the TR pair-wise correlation matrix W_{ij} of size $N \times N = 386 \times 386$ that was generated using the generalized Jaccard similarity. MWCP solution can give important information about what TR clusters are involved in specific functions within the cell, including leukaemia or immune system-related functions (pathways). The KEGG [29] pathways analysis can be used to interpret the cellular functions of identified TR cooperation in K562 cells (see Table S11 from [27]).

DOMINO was applied to identify the maximum weighted clique (MWC) based on the mean Jaccard index within the 3DCoop-generated gene-gene interaction network. Starting with 100 different random initial conditions, our solver successfully found MWC with 20% success probability. At the same time, BFGS had only 3% success probability of solving Eq. (1) on the same set of initial conditions. The found maximum weighted clique (CBX3-CTCF-JUND-MAZ-RAD21-RESTSMC3-ZNF143) is depicted in Fig. 3 along with the most enriched pathways associated with it, which agrees with the findings of [27] (see Table S4 and Fig. 2B). The KEGG pathway analysis of detected MWC encompasses multiple pathways related to hematopoietic cancers. This finding

implies that this collaboration of TRs may play a role in cell type-specific gene regulation within leukaemia by influencing the 3D chromatin organization [30].
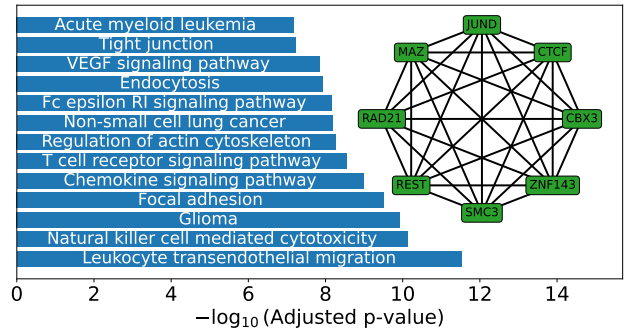

Figure 3. Thirteen most important KEGG pathways for ((CBX3-CTCF-JUND-MAZ-RAD21-RESTSMC3-ZNF143)) cluster identified as an MWC in the network of 386 Transcriptional Regulators detected in K562 human myelogenous leukaemia cell line using 3DCoop pipeline. Inset illustrates the most important Maximum Clique subnetwork found in the genes coexpression network of size $N = 386$ from [27]. Green nodes correspond to TRs highlighted by our solver. Calculations were performed with parameters: $\xi = 5$, $T = 20$, and $dt = 2 \cdot 10^{-4}$

Identifying and ranking all cliques within a network based on their weights involves repeatedly applying MWC detection using DOMINO. After detecting an MWC, its vertices are iteratively deleted to form a new subnetwork, allowing the search for a new MWC to continue. This process is repeated for each clique found in the previous steps. To avoid redundant detections of the same clique, we keep track of the cliques already discovered and rank them according to their weights.

Indirect correlations. DOMINO uses the condensate amplitudes to identify the most connected subsets in the network. In complex networks, direct connections may not exist between two nodes, but they can still exhibit correlations through other intermediary nodes and edges. These indirect correlations (indirect interactions) arise from various mechanisms like shared inputs/outputs, common regulatory factors, or feedback loops. Understanding and detecting these indirect correlations offer valuable insights into the network's structure and functionality. Once MWC is identified within a network, the phases of the oscillators in a complex-valued oscillatory network can be utilized to uncover both direct and inverse correlations among the network elements. To accomplish this, one can apply the original optical system, as outlined in Eq. (2), which incorporates saturable nonlinearity, alongside the feedback mechanism described in Eq. (3), designed to minimize the XY Hamiltonian. In this context, the coupling strengths between oscillators can be either positive or negative. The extent of indirect correlations between nodes is inferred from the magnitude of their phase differences as depicted in Fig. 4: a more significant phase disparity implies a stronger neg-
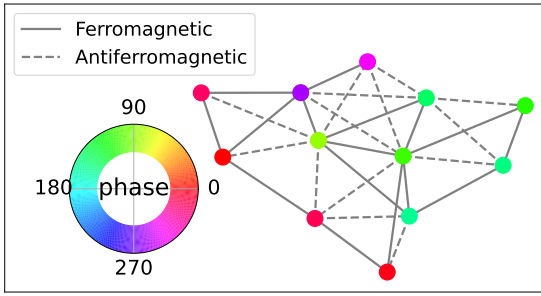
Figure 4. The indirect positive and negative correlations obtained by minimizing the XY Hamiltonian using the temporal evolution of Eq. (2) with Eq. (3) and $\epsilon = 0.1, \gamma_{\text{inj}}^{(i)}(0) = -10$. Solid edges between pairs of vertices i and j of the shown network represent ferromagnetic couplings $J_{ij} = +1$, and the dashed edges correspond to anti-ferromagnetic couplings $J_{ij} = -1$. Pairs of vertices not connected by edges have zero couplings $J_{ij} = 0$. Colors indicate the phases of ψ_i and reveal indirect correlations between the nodes.

ative correlation. This method provides a systematic approach to evaluate the correlation strengths within the network.

Conclusion. We have developed the optical platform DOMINO, a form of PNNs, for detecting maximum-weighted subnetworks within extensive networks and the indirect correlation between the nodes. This approach demonstrates several key potential advantages when implemented in optical hardware, including low energy consumption, rapid operational speed, high convergence rates towards optimal solutions, and noise resilience, an inevitable factor in real-world physical systems. Our results indicate that DOMINO outperforms contemporary optimization tools like Gurobi regarding speed and confidence in finding optimal solutions. The effectiveness of DOMINO on real complex networks and its ability to reveal indirect correlations highlights the promising potential of this platform in social studies, finance, medicine, logistics, etc.

[1] S. K. Vadlamani, T. P. Xiao, and E. Yablonovitch, Proceedings of the National Academy of Sciences **117**, 26639 (2020).

[2] P. L. McMahon, A. Marandi, Y. Haribara, R. Hamerly, C. Langrock, S. Tamate, T. Inagaki, H. Takesue, S. Utsunomiya, K. Aihara, *et al.*, Science **354**, 614 (2016).

[3] T. Inagaki, Y. Haribara, K. Igarashi, T. Sonobe, S. Tamate, T. Honjo, A. Marandi, P. L. McMahon, T. Umeki, K. Enbutsu, *et al.*, Science **354**, 603 (2016).

[4] Y. Yamamoto, K. Aihara, T. Leleu, K.-i. Kawarabayashi, S. Kako, M. Fejer, K. Inoue, and H. Takesue, npj Quantum Information **3**, 1 (2017).

[5] T. Honjo, T. Sonobe, K. Inaba, T. Inagaki, T. Ikuta, Y. Yamada, T. Kazama, K. Enbutsu, T. Umeki, R. Kasahara, *et al.*, Science advances **7**, eabh0952 (2021).

[6] M. Babaeian, D. T. Nguyen, V. Demir, M. Akbulut, P.-A. Blanche, Y. Kaneda, S. Guha, M. A. Neifeld, and N. Peyghambarian, Nature communications **10**, 1 (2019).

[7] V. Pal, S. Mahler, C. Tradonsky, A. A. Friesem, and N. Davidson, Physical Review Research **2**, 033008 (2020).

[8] M. Parto, W. Hayenga, A. Marandi, D. N. Christodoulides, and M. Khajavikhan, Nature Materials **19**, 725 (2020).

[9] D. Pierangeli, G. Marcucci, and C. Conti, Physical Review Letters **122**, 213902 (2019).

[10] C. Roques-Carmes, Y. Shen, C. Zanoci, M. Prabhu, F. Atieh, L. Jing, T. Dubček, C. Mao, M. R. Johnson, V. Čeperić, *et al.*, Nature Communications **11**, 249 (2020).

[11] N. G. Berloff, M. Silva, K. Kalinin, A. Askitopoulos, J. D. Töpfer, P. Cilibrizzi, W. Langbein, and P. G. Lagoudakis, Nature Materials , 1120–1126 (2017).

[12] K. P. Kalinin, A. Amo, J. Bloch, and N. G. Berloff, Nanophotonics **9**, 4127 (2020).

[13] M. Vretenar, B. Kassenberg, S. Bissesar, C. Toebes, and J. Klaers, Physical Review Research **3**, 023167 (2021).

[14] A. Lucas, Frontiers in physics **2**, 5 (2014).

[15] F. Khosravi, A. Scherer, and P. Ronagh, *2023 IEEE International Conference on Quantum Computing and Engineering (QCE)*, **01**, 184 (2023).

[16] F. Khosravi, U. Yildiz, A. Scherer, and P. Ronagh, arXiv preprint arXiv:2209.04415 (2022).

[17] K. Kalinin, G. Mourgias-Alexandris, H. Ballani, N. G. Berloff, J. H. Clegg, D. Cletheroe, C. Gkantsidis, I. Haller, V. Lyutsarev, F. Parmigiani, L. Pickup, *et al.*, arXiv preprint arXiv:2304.12594 (2023).

[18] B. Amgalan and H. Lee, PloS one **9**, e104993 (2014).

[19] S. Cai and J. Lin, in *Proceedings of the Twenty-Fifth International Joint Conference on Artificial Intelligence*, IJCAI'16 (AAAI Press, 2016) p. 568–574.

[20] T. S. Motzkin and E. G. Straus, Canadian Journal of Mathematics **17**, 533 (1965).

[21] K. P. Kalinin and N. G. Berloff, Phys. Rev. B **100**, 245306 (2019).

[22] K. P. Kalinin and N. G. Berloff, New Journal of Physics **20**, 113023 (2018).

[23] T. Yagafarov, D. Sannikov, A. Zasedatelev, K. Georgiou, A. Baranikov, O. Kyriienko, I. Shelykh, L. Gai, Z. Shen, D. Lidzey, and P. Lagoudakis, Communications Physics

3, 18 (2020).

[24] C. Schneider, A. Rahimi-Iman, N. Y. Kim, J. Fischer, I. G. Savenko, M. Amthor, M. Lermer, A. Wolf, L. Worschech, V. D. Kulakovskii, *et al.*, Nature **497**, 348 (2013).

[25] J. D. Töpfer, H. Sigurdsson, L. Pickup, and P. G. Lagoudakis, Communications Physics **3**, 2 (2020).

[26] Gurobi Optimization, LLC, (2023).

[27] X. Yi, Z. Zheng, H. Xu, Y. Zhou, D. Huang, J. Wang, X. Feng, K. Zhao, X. Fan, S. Zhang, X. Dong, Z. Wang, Y. Shen, H. Cheng, L. Shi, and M. J. Li, Science **24**, 103468 (2021).

[28] E. Klein, F. Vánky, H. Ben-Bassat, H. Neumann, P. Ralph, J. Zeuthen, and A. Polliack, International Journal of Cancer **18**, 421 (1976).

[29] "Kegg pathway database," `https://www.genome.jp/kegg/pathway.html`.

[30] J. Hou, G. Scalcinati, M. Oldiges, and G. N. Vemuri, Applied and Environmental Microbiology **76**, 851 (2010).

[31] M. Matuszewski, A. Prystupiuk, and A. Opala, Phys. Rev. Appl. **21**, 014028 (2024).

I. SUPPLEMENTAL MATERIALS

A. Generation of coupling strengths

To generate coupling strengths J_{ij} corresponding to random networks of size N and network density p we first chose random partitions $\{n_i\}_N$ of integer number N s.t. $N = \sum_i n_i$ with $3 \le n_i \le 6$ and create $|\{n_i\}_N|$ cliques of respective sizes n_i containing $E_i = n_i(n_i - 1)/2$ connections respectively. Then we generate $S = pN(N - 1)/2 - \sum_i E_i$ random connections between nodes belonging to different cliques and assign random weights $J_{ij} \in (0, 1]$ to each connection (i, j) of the resulting network. The resulting graph will represent a connected network of size N and density p containing randomly generated cliques of different sizes n_i.

B. DOMINO properties on random networks

In this section, we demonstrate the performance of the DOMINO solver and its comparison with the Gurobi solver for random networks with coupling strengths J_{ij} being randomly generated from a uniform distribution by $J_{ij} = \eta_{i<j}(p) + \eta_{i<j}^T(p)$, where $\eta_{i<j}(p)$ is a random upper triangular matrix with entries $\eta_{i<j} \in [-1, 0) \cup (0, 1]$ generated uniformly with probability $p < 1$ and $\eta_{i<j} = 0$ with probability $1 - p$. Thus, matrix **J** describes the connectivity of a weighted undirected network in which vertices i and j are connected by an edge of weight $\eta_{i<j}$ with probability p. We refer to parameter p as the network density. We selected only matrices corresponding to connected networks when generating **J**. Fig. 5 illustrates the accumulated probability of success as a function of the execution time for the DOMINO and Gurobi solvers.

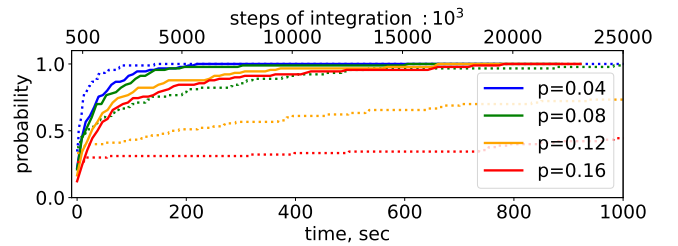Fig. 6(a) depicts histograms obtained from computer

Figure 5. Comparison of the accumulated probability of success as a function of TTS (Time to Solution) for Gurobi (dotted lines) and the DOMINO solver (solid lines) governed by Eq. (6) of the main text with $\xi = 5$ and $dt = 0.0002$. Both solvers were executed on the same single CPU core. DOMINO computation time was estimated as the time required to sequentially execute solver 100 times, each starting with different initial conditions. The upper axis shows the corresponding total number of steps of numerical integration. The probability of success at each time step for both solvers was estimated as the fraction of 90 different matrices **J** for which the global minimum was found.

simulations of DOMINO solver (Eq. (6) of the main text) and compares them with those found by 'BFGS' algorithm implemented via the built-in 'scipy. optimize' library, as well as with solutions derived from the leading eigenvectors of the weights matrix **J** specified in this section. Figure 7 demonstrates the growth in characteristic time required by the DOMINO solver to achieve a steady state with the network size N growth.

C. Noisy data

In this section, we demonstrate the system's robustness to noise and imperfections of the implemented couplings that unavoidably occur in the real setup due to the imperfection of pumping and overlapping condensates. We simulate the fluctuations of the couplings J_{ij} from required values implementing noise of level σ and solve numerically Eq. (6) of the main text with the coupling strengths $J_{ij}^{\text{noisy}}(G) = J_{ij}(G) + \sigma\zeta_{ij}(t)$, where $\zeta_{ij}(t) \in (0, 1]$ represents time-varying random noise of level σ. To assess the system's resistance to internal noise, we compare $H_{\text{loss}} = -\frac{1}{2}\sum_{i,j}|J_{ij}|(\psi_i\psi_j^* + c.c.)$ with $H_{\text{loss}}^{\text{noisy}} = -\frac{1}{2}\sum_{i,j}|J_{ij}^{\text{noisy}}|(\psi_i\psi_j^* + c.c.)$ for different steady states ψ_i and different noise levels σ. Figure 8 shows that DOMINO remains noise resistant up to $\sigma \sim 1/2$.

D. Efficiency estimates

To estimate the physical time and power required by the real optical system to solve optimization problem Eq. (1) of the main text, we consider the complex Ginzburg-Landau equation in dimensional form, which accurately describes the dynamics of exciton-polariton
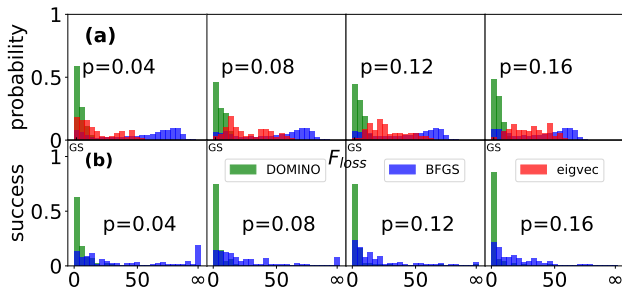
Figure 6. (a) Histograms of the solutions found by DOMINO Eq. (6) of the main text (green) and using 'BFGS' algorithm (blue). The histograms were calculated based on 100 random networks of size $N = 100$ with different weight matrices $\mathbf{J}$ generated as described in this section, using 100 different initial conditions for each matrix $\mathbf{J}$. The red bars represent the solutions defined by the leading eigenvectors of $\mathbf{J}$. The leftmost bars correspond to the global minima, verified for each graph using the Gurobi solver. (b) Number of different random initial conditions required to find the optimal solution using numerical integration of Eq. (6) calculated for 100 different connected random networks of size $N = 100$ for different network densities p. Green bars correspond to solutions found by the DOMINO solver described in Eq. (6) of the main text, and blue bars demonstrate the convergence rates of the 'BFGS' algorithm. The values corresponding to ∞ indicate the fraction of networks for which the ground state was not found for any of the 100 different initial conditions used.
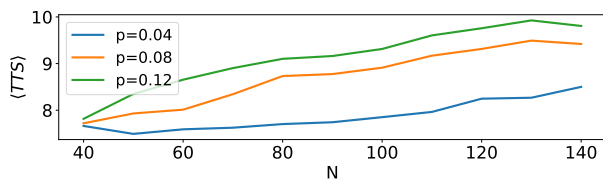

Figure 7. Average dependence of time required to find steady state by Eq. (6) of the main text with $\xi = 5$ and $dt = 1 \cdot 10^{-4}$ on the size of the system. $\langle TTS \rangle$ was estimated as the average TTS of 10 executions of the solver with different random initial conditions per each of 90 different matrices $\mathbf{J}$ of sizes N and corresponding network densities p. A detailed description of $\mathbf{J}$'s structure for each graph of given density p is given in Supp. Mat A.

condensates

$$i\hbar \frac{\partial \tilde{\Psi}}{\partial \tilde{t}} = -\frac{\hbar^2}{2m} \tilde{\nabla}^2 \tilde{\Psi} + U_0 |\tilde{\Psi}|^2 \tilde{\Psi} + \frac{i\hbar}{2} \left(P_{\text{inj}} - \gamma_c \right) \tilde{\Psi}, \quad (7)$$

where $P_{\text{inj}} = R_R P / (\gamma_R + R_R |\tilde{\Psi}|^2)$ is gain, R_R is relaxation rate of excited particles from reservoir, U_0 is strength of delta-functional polariton-polariton interactions, γ_R - linear losses of excited particles. The dimensionless Eq. (2) of the main text can be obtained by transformations: $\tilde{\Psi} \rightarrow \sqrt{\hbar^2/2mU_0 l^2}\Psi$, $\tilde{r} \rightarrow lr$, $\tilde{t} \rightarrow 2mtl^2/\hbar$ with subsequent tight-binding approximation. Now we can estimate $T_{\text{real}} = 2mTl^2/\hbar$ as real optimization time required by purely optical setup, where $m \approx 10^{-4} \div 10^{-5} \, m_e$ is the polariton mass, m_e is the electron mass and $l = 1 \, \mu m$
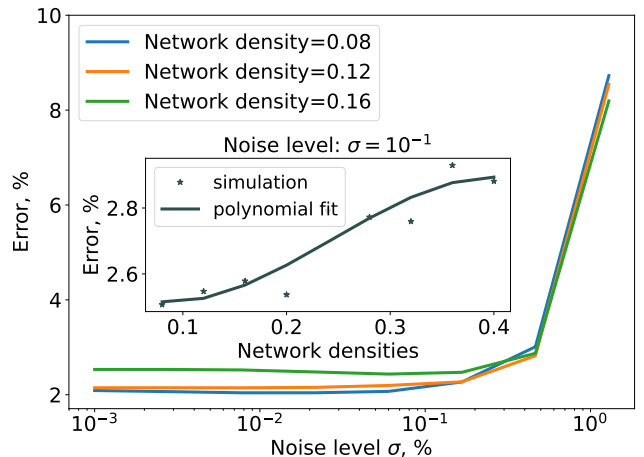

Figure 8. Robustness of DOMINO to noise. Equation 6 of the main text was solved numerically and averaged over 500 different connected networks G of size $N = 30$ as described in Supp. Mat. A. for network density p with 100 different initial conditions per each network and weights matrices $\mathbf{J}(G)$ perturbed by random time-varying uniform noise $\sigma \zeta_{ij}(t)$ of level σ as $J_{ij}^{\text{noisy}}(G) = J_{ij}(G) + \sigma \zeta_{ij}(t)$. Here $\zeta_{ij}(t) = 0$ if vertices i and j are not connected in G and $\zeta_{ij} \in (0, 1]$ otherwise. The error represents the deviation of the loss function H_{loss} of the solution of a noisy system from a system without noise. It was calculated as: Error $= (H_{\text{loss}}^{\text{noisy}} - H_{\text{loss}})/(H_{\text{loss}}^{\text{noisy}} + H_{\text{loss}})$, where $H_{\text{loss}}^{\text{noisy}}$ is the loss function of the solution calculated with the noise introduced to $J_{ij}(G)$. The inset shows the corresponding errors depending on the network density for fixed noise level $\sigma = 10^{-1}$.

is the characteristic unit length. For dimensionless time $T = 100$ per one run for one initial condition, we find $T_{\text{real}} \approx 270 \, ps \div 2.7 \, ns$. We must emphasise that time T and T_{real} that one single run on purely optical solver takes also grows with the size of the problem N as shown in Fig. 7. However, it scales much slower in contrast to conventional von Neuman architectures because optical systems do not waste additional time performing arithmetic operations, the number of which grows in proportion to the number of edges $\sim O(N^2)$ with the growth of the network size N.

The real energy cost E_{real} of the real purely optical solver that executes DOMINO scales linearly with N and does not depend on the number of edges because interactions occur via overlapping of the condensates, each created by the laser beam. Therefore E_{real} can be estimated as $E_{\text{real}} \sim \text{const} \cdot \hbar^2 \gamma_{\text{inj}} N / (2ml^2) \sim O(N)$. Exciton-polariton systems, a prime example of coupled light-matter condensates, are particularly energy-efficient because they require energy only to create and maintain N overlapping condensates. In contrast, electronic and optoelectronic solvers consume energy for every edge: $E_{\text{electronic}} \approx E_{\text{el}} \cdot p \cdot N(N-1)/2 \sim O(N^2)$. Where $E_{\text{el}} = 1 \, pJ$ is the unit energy per operation consumed by the elec-

tronic system [31], and p is a network density.